Numerical evaluation of CRORs dynamic loads induced by whirl flutter

A Dugeai, S Verley

Numerical evaluation of CRORs dynamic loads induced by whirl flutter

A.Dugeai[1], S.Verley[1]

1 Onera – The French Aerospace Lab
F-92322 Châtillon, FRANCE
simon.verley@onera.fr, alain.dugeai@onera.fr

Keywords: open-rotor, whirl flutter, aeroelasticity, Navier-Stokes, mesh deformation.

Abstract: This paper presents an innovative approach to simulate rigid motions of Counter-Rotating Open-Rotors using the *elsA* ONERA solver. The goal of these simulations is to evaluate unsteady aerodynamic forces on the aircraft encountering engine system vibrations, and to deliver aerodynamic data for whirl flutter analysis of CRORs.

NOMENCLATURE

$(x, y, z), (\vec{x}, \vec{y}, \vec{z})$	coordinates and base vectors in rotating frame
$(X, Y, Z), (\vec{X}, \vec{Y}, \vec{Z})$	coordinates and base vectors in absolute frame
(ϕ_R^P, ϕ_R^Y)	pitch and yaw modes in relative frame
(ϕ_A^P, ϕ_A^Y)	pitch and yaw modes in absolute frame
(ϕ_R^*, ϕ_A^*)	complex mode in relative and absolute frames
Ω, ω	rotation and vibration pulsations
$\vec{r}$	current point location vector
Φ	deformation mode shapes
M, D, K	structural mass, damping, stiffness matrices
$\mu_s, \beta_s, \gamma_s, G$	generalized structural mass, damping, stiffness matrices and gyroscopic damping matrix
J_X	axial moment of inertia
q	generalized coordinates
$F_A(t)$	aerodynamic force
α, β	incidence, sideslip angle
γ	blade pitch angle
ψ	azimuth angle
ψ_b^0	blade b azimuth in propeller frame
α_b	blade b incidence
ε	velocity corrective term for nacelle incidence effect
w	velocity corrective term for front blade wake effect
N_{Front}, N_{Aft}	front and aft propellers blade number

1 INTRODUCTION

In the global objective of reducing the impact of aeronautical systems on environment, very stringent constraints are put on Aircraft and Engine manufacturers in order to meet ACARE 2020 objectives, in terms of noise reduction and energetic efficiency. Compared to 2005 figures, the target levels of emission reduction are as high as 50% for CO_2, 80% for NO_x and 50% in terms of noise emission. In this context, a massive effort is put by engine and aircraft manufacturers on alternative propulsion concepts, such as counter-rotating open rotors, which seem to be promising especially in terms of fuel efficiency. These systems offer a bypass ratio around 60 and are thus about 30% more fuel efficient than current jet engines, although they may operate at lower cruise speed.

One main issue, however, seems to be the noise and vibrations levels emitted by such systems during flight. So, on the one hand a large research effort is developed in order to reduce noise levels, mainly due to wake interactions, and on the other hand, specific studies are started in order to evaluate vibration levels generated by CROR engines.

The present study focuses on the latter issue. This paper presents some recent results obtained at ONERA with the *elsA*[1] solver, in order to simulate the phenomenon of whirl flutter on CROR systems. This phenomenon due to fluid-structure interaction between the supporting wing/pylon structure and the unsteady aerodynamic loads is likely to occur on propellers and CRORs, and may

lead to unstable behaviours, which must be investigated.First accidents were recorded in the late 50es when two Lockheed Electra encountered divergent whirl flutter phenomena, leading to the crash of both aircrafts. This unstable phenomenon was identified as being linked to a previous damage to the wing structure. This damage leads to the modification of the wing modal frequencies and to a coupling with the propeller gyroscopic flutter mode.

The purpose of this paper is to provide High Fidelity numerical solutions to evaluate the aerodynamic forces encountered by a CROR in whirl flutter motion.

2 AERODYNAMIC SOLVER *ELSA*

The present work has been carried out using ONERA's aerodynamic solver *elsA*. This project has been initiated in 1997 within the ONERA's aerodynamic department, and is now being developed by a large number of contributors from several departments inside ONERA, but also by industrial or academic partners, such as AIRBUS, SAFRAN, CERFACS, ECL/LMFA and CENAERO.
elsA is a multipurpose multiblock structured code dedicated to the aerodynamic simulations of external and internal flows for aircraft, turbomachinery, helicopter, propellers applications.

2.1 *elsA* aerodynamic solver features

elsA allows aerodynamic computations for compressible viscous and inviscid flows. It handles RANS and URANS equations with a large set of turbulence models ranging from algebraic to turbulent transport equations, including DRSM, DES and LES models which are now being implemented for some applications. Transition criteria are also available, including Menter transport equation model. Considering the meshing strategy, *elsA* is basically a multiblock structured grid solver. Blocks joins may be totally or partially coincident. *elsA* can also handle chimera overset grids. Patched grid and overset Chimera grids techniques may be implemented to overcome multiblock structured grids meshing issues for complex geometrical configurations. Hybrid structured/unstructured meshes capabilities are now also under development. Motion and deformations of bodies may be taken into account for steady/unsteady applications. The finite volume approach is used for spatial discretization in connection with centered or upwind schemes (Jameson, Roe, Van Leer). Runge-Kutta or backward Euler time schemes are available. Local, global, dual and gear time stepping schemes are implemented. Convergence may be accelerated using implicit techniques (IRS, LU factorization) and/or multigrid resolution schemes. Considering rotating machinery problems, relative frame with either relative or absolute variables formulations may be used (turbomachinery, helicopter, propellers). Parallelization is achieved through the distribution of mesh blocks over a set of processors. As far as unsteady computations are concerned, *elsA* is able to handle mesh deformation using an ALE formulation of flow equations.

2.2 *elsA* aeroelastic module

The fluid-structure problem can be formulated as a coupled field problem, where the solutions are coupled only at the boundary interfaces between the fluid and the structure. It is then possible to run separate solvers for the flow computation and the structure computation, and to reach a coupled solution by exchanging information at the common fluid-structure boundaries. However, in most aeroelastic problems, the structure may be assumed to be linear. In this case, it is much easier and more efficient to extract the structural information from a full finite element model in a pre-processing step and to solve the mechanical system directly in the aerodynamic code. This strategy has been adopted to extend the aerodynamic *elsA* solver for fluid-structure coupling.

A general framework has been developed in the optional "Ael" subsystem of *elsA* ([2], [3], [4]) over the last few years, in order to extend *elsA* to different kinds of static or unsteady aeroelastic simulations (Figure 1).

The purpose of these simulations is the prediction of the in-flight static or dynamic behavior of flexible aerodynamic structures and their aeroelastic stability. This "Ael" subsystem gives access in a unified formulation to different types of aeroelastic simulations, compatible with the flow solver features. The available simulations include non-linear and linearized harmonic forced motion

computations, static coupling and consistent dynamic coupling simulations in the time-domain. Various levels of linear structural modelling are available ("reduced flexibility matrix" for static coupling, modal approach, or full finite element structural model). In addition to the specific aeroelastic simulation driver, the *elsA*/Ael module basically integrates three main subsystems: a module for data transfer between CFD and CSD solvers, an integrated static and dynamic linear structural solver and a 3D fluid mesh deformation tool. Transfer of displacements and loads between the structure and the fluid are based on the exchange of generalized coordinates and forces for the modal approach, whereas it uses specific interpolation or smoothing techniques, the nearest neighbor or virtual work principle based techniques for the finite element approach. Concerning the important issue of 3D fluid mesh deformation, several methods are currently implemented such as described in the next paragraph.

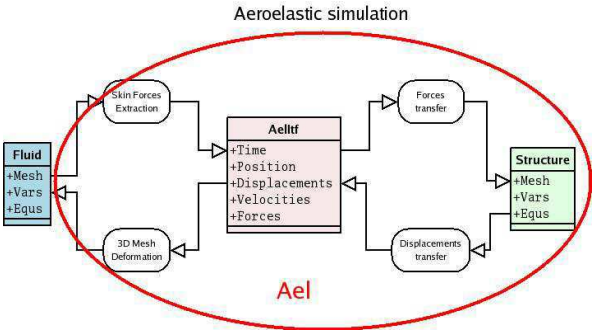

Figure 1 - *elsA*/Ael aeroelastic subsystem

Time consistent unsteady aeroelastic simulations are conducted using dual time stepping or Gear methods. These dynamic aeroelastic simulations may be either weakly coupled or strongly coupled.
In the weak coupling case, the motion of the structural model is prescribed as a single harmonic motion or a combination of harmonic motions, which can be rigid ones or following its natural vibration modes Φ. The computation is run over several periods of vibration in order to get the unsteady aerodynamic response to the forced motion of the structure. The aerodynamic temporal response of the fluid gives access to unsteady pressure distributions on the model surface, and may be integrated to get unsteady aerodynamic loads over the structure. In the purpose of linear stability analysis for flutter, these pressure distributions may be projected on the modal basis shapes, to get unsteady generalized aerodynamic forces $\Phi^t F_A(t)$ which are prescribed on the right hand side of the modal projected structural dynamics equation:

$$\Phi^t M \Phi \ddot{q} + \Phi^t D \Phi \dot{q} + \Phi^t K \Phi q - \Phi^t F_A(t) = 0$$

A first harmonic analysis of the unsteady forces is performed to study in the frequency domain the aeroelastic stability of the fluid-structure coupled system. Flutter response is classically analysed using p-k stability method. In the strong coupling case, the structural dynamics equation is solved in the time domain during the unsteady aerodynamic computation, using a Newmark resolution scheme. At each physical time step, aerodynamic forces and elastic forces are balanced using an additional coupling loop and the procedure gives access to the unsteady evolutions of the structural variables and of the aerodynamic field as well. Only the weak coupling method is implemented in this paper.

2.3 Mesh deformation capabilities for aeroelastic simulations

The *elsA/Ael* aeroelastic module implements several mesh deformation techniques. The present work uses a linear elastic continuous material analogy method. A 8-node hexahedral finite element approach is used to discretize the aerodynamic grid mesh deformation problem. The local stiffness matrix is computed approximately, using a one point Gauss integration procedure, specifically corrected for Hour-glass spurious modes treatment. The static equilibrium of the discretized system leads to the following linear system:

$$K_{ii}\, q_i = -K_{if}\, q_f$$

where q_i and q_f are respectively the computed and boundary prescribed displacement vectors.

As the stiffness matrix is positive definite, the system is solved using a pre-conditioned conjugated gradient method. For *elsA*, the technique is implemented in the case of multi-block structured grids.

The full mesh deformation is defined as a sequence of individual block deformations. Boundary conditions are set to impose zero or prescribed displacement values, to move on a plane, on the local surface boundary or along or normally to a prescribed vector, and to get deformations continuity through block interfaces. In order to fulfil boundary conditions, the conjugated gradient algorithm is modified. The resolution procedure is kept compatible with the boundary conditions in iteratively projecting the solution and search direction vectors in the proper linear subspace. However, performing structural static deformation computations on the full aerodynamic grid is expensive, and reduction techniques are implemented in order to solve the structural problem on a coarse grid, by packing cells, especially in the boundary layer regions where the aerodynamic discretization is extremely dense.

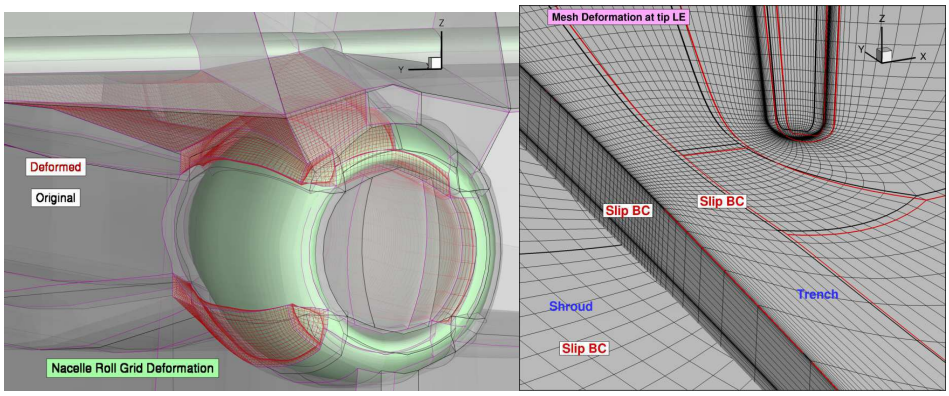

Figure 2 - Mesh deformation examples using elastic analogy: oscillating nacelle (a), axial compressor with trench clearance at shroud (b)

The structural analogy method is very versatile and is used for a large range of applications: turbomachines, aircrafts, helicopter, propellers and here, CRORs. The implemented mesh deformation procedure has been validated for use with chimera grids, and is now being fully parallelized in the current *elsA* version.
An alternate mesh deformation technique based on TransFinite Interpolation (TFI) is also available in *elsA/Ael*, but has not been implemented in the present work.

3 RIGID MOTION CROR SIMULATIONS

The objective of this study is to evaluate the aerodynamic forces which occur on a counter-rotating open-rotor in forced rigid motion of whirl flutter. As presented in [5], the motion of the nacelle and propellers may be in a linear approximation prescribed in the relative rotating frame in terms of rotating modes of deformation of the structure. This procedure is valid either for static incidence or sideslip effects, or for unsteady pitch and yaw modes or whirl flutter.

3.1 Deformable grid approach

An original approach is implemented here to prescribe this kind of forced motion of the structure.

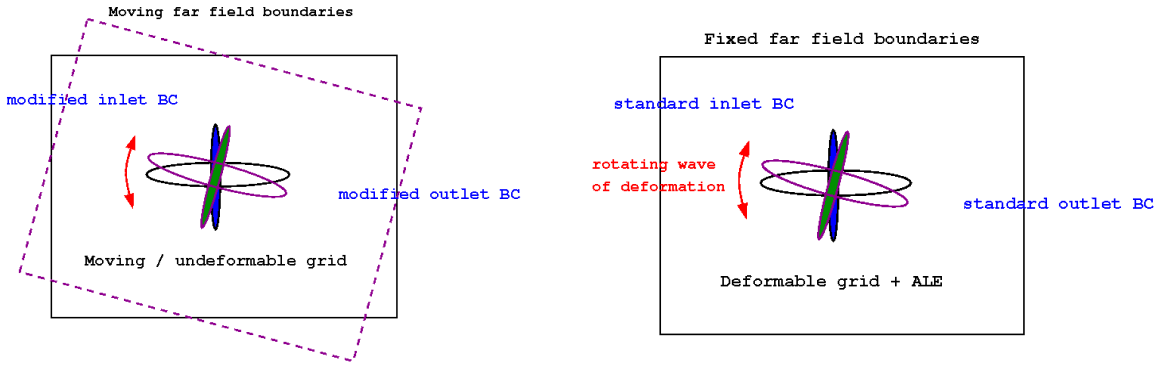

Figure 3 : Alternate procedures for forced motion accounting

Instead of using a moving/undeformable block approach, which would require the implementation of specific entrainment velocity and far field boundary conditions formulations, this work uses a deformable grid approach to take into account the engine rigid forced motion (Figure 3). Therefore,

even though 3D mesh deformation and ALE formulation for the flow resolution are required, far field boundaries are left unchanged.
The main advantage of this technique is that it's quite similar to that already implemented in the *elsA* software concerning aeroelastic damping prediction of turbomachines blade vibration modes using the weak coupling approach (as detailed in 2.2), which is today widely used at ONERA and SAFRAN. An additional benefit of this procedure is to be able to account for potential flexible modes of deformation of the structure in the same way, without any additional development.

3.2 Rotating modes in relative frame

Deformation of the structure must be defined in the relative frame, where the aerodynamic grid is defined. The current paragraph summarizes the way deformations in the relative frame are to be defined in order to get the targeted global motion in the absolute frame.

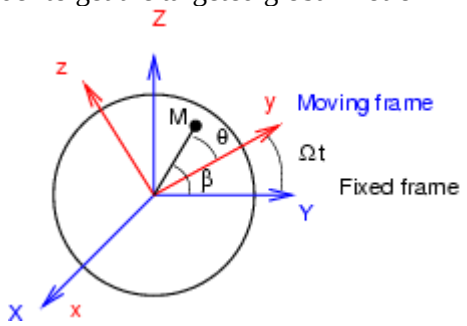

$$\vec{y} = \vec{Y}\cos\Omega t + \vec{Z}\sin\Omega t$$
$$\vec{z} = -\vec{Y}\sin\Omega t + \vec{Z}\cos\Omega t$$
$$\vec{x} = \vec{X}$$
$$\vec{y} - j\vec{z} = e^{j\Omega t}(\vec{Y} - j\vec{Z})$$

Figure 4 : Rotating frame axes

In a linear approximation, pitch and yaw modes (with rotation axes at origin) in the relative frame may be expressed as follows:

$$\phi_R^P = z\vec{x} - x\vec{z} = -\vec{r}\times\vec{y}$$
$$\phi_R^Y = y\vec{x} - x\vec{y} = \vec{r}\times\vec{z}$$

Using a complex algebra we may introduce $\phi_R^* = \phi_R^P + j\phi_R^Y$. The following relation between complex deformation shape expressed in relative and absolute frames holds:

$$\phi_R^* = -\vec{r}\times(\vec{y} - j\vec{z}) = -\vec{r}\times(\vec{Y} - j\vec{Z})\, e^{j\Omega t} = \phi_A^* e^{j\Omega t}$$

Therefore, static incidence (respectively sideslip) in the absolute frame read in relative frame coordinates as follows:

$$u_{Inc} = \alpha\phi_A^P = \alpha\,\mathrm{Re}\left(\phi_R^* e^{-j\Omega t}\right) \quad u_{Side} = \beta\phi_A^Y = \beta\,\mathrm{Re}\left(-j\phi_R^* e^{-j\Omega t}\right)$$

In the unsteady case, pitch and yaw motion are given by a harmonic modulation in time of the rotating mode formulation derived here above.

$$u_{Pitch} = \alpha\cos\omega t\,\mathrm{Re}\left(\phi_R^* e^{-j\Omega t}\right)$$

The whirl flutter mode corresponds to a combination of pitch and yaw modes in quadrature, which reads:

$$u_{WF} = \alpha\,\mathrm{Re}\left((\cos\omega t + j\sin\omega t)\,\phi_R^* e^{-j\Omega t}\right)$$
$$u_{WF} = \alpha\,\mathrm{Re}\left(\phi_R^* e^{-j(\Omega-\omega)t}\right)$$

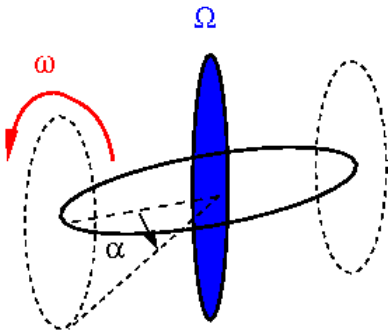

4 AIRBUS GENERIC CROR CONFIGURATION 7 APPLICATION

The test case implemented in this paper is the Airbus AIPX7 generic counter-rotating open rotor configuration. This CROR has a 11-blade front propeller and a 9-blade aft propeller. The configuration has been studied in the case of cruise conditions (low transonic). The implemented structured multiblock grid is a full 360° model. The total number of blocks is 220 (11 blocks per

blade). The grid has more than 24 million cells. In order to deal with counter-rotation, a chimera overlap is located in the inter-propeller region. The configuration is fully described in a CGNS compliant data base, which is processed by the *elsA* solver for steady and unsteady aeroelastic simulations. Pre and post-processing are fully automated.

4.1 Chimera overset grids modelling for counter-rotating open rotor

The current CROR configuration is modelled here for the purpose of unsteady aerodynamic simulations using chimera overset grids to account for both counter rotating propellers. An overlap region between backward rotating blocks (front region) and forward rotating blocks (aft region) is located between both propellers as shown on Figure 5. The *elsA* solver is implemented with chimera grids, in relative frame and absolute velocities formulation. At each physical time step, interpolation coefficients are re-computed to take into account counter rotation of overlapping front and aft blocks.

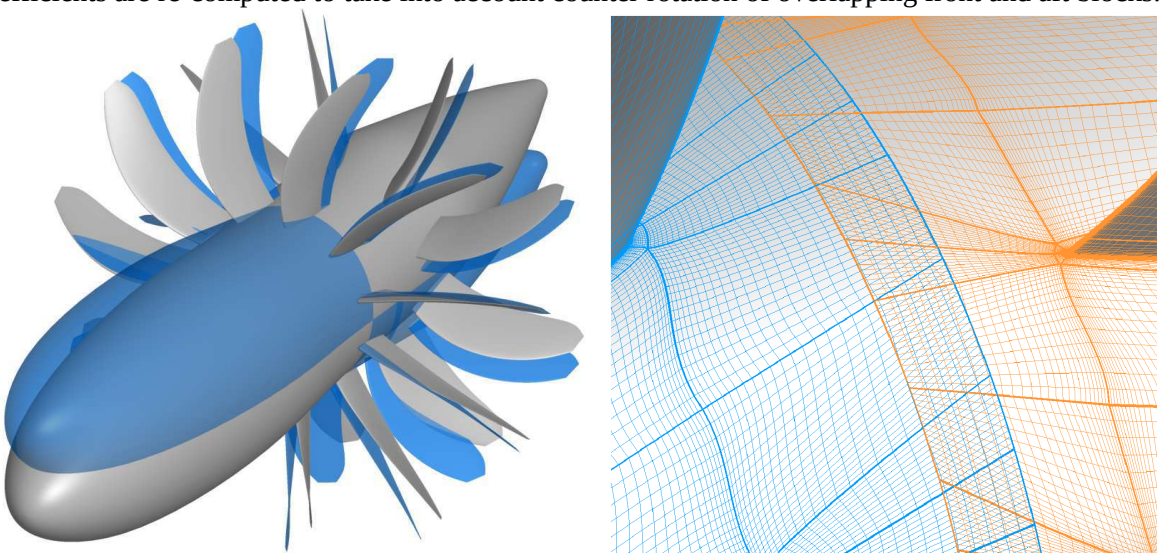

Figure 5 : AIPX7 model: pitch mode (blue) and grid overlap between propellers

As developed above, the rigid motion of the CROR is implemented using a deformation mode in relative rotating frame approach. However, in the CROR case, front and aft blocks are counter-rotating. Therefore, two different complex excitation modes in both different rotating frames are needed to model the same global motion in the absolute frame.
For example in the case of whirl flutter motion we have:

$$u_{WF\_Front} = \alpha \,\mathrm{Re}\left(\phi_R^* e^{-j(\Omega_{Front}-\omega)t}\right) \quad u_{WF\_Aft} = \alpha \,\mathrm{Re}\left(\phi_R^* e^{-j(\Omega_{Aft}-\omega)t}\right) \quad \Omega_{Aft} = -\Omega_{Front}$$

4.2 Generic numerical setup

The unsteady computations are using the following main parameters:

- Gas model: Perfect gas
- Viscosity: Sutherland
- Turbulent model: Spalart-Allmaras
- Time step: equivalent of 1°
- Spatial scheme: Jameson
- Time scheme: Backward-Euler with implicit phase LU-SSOR (using Dual Time Step technique)

Several unsteady simulations have been performed, for which 150h on 64 cpu cores are required for each of them in order to reach an acceptable level of convergence:

- static incidence effect
- unsteady axial pumping effect
- pitch at several frequencies
- forward and backward rotating whirl flutter

For confidentiality reason, all force values presented are given in percent of the total thrust of the CROR at cruise condition.

4.3 Static incidence effect

In order to validate the approach and the implementation, the “deformable mesh” approach described above has been used to simulate the effect of a static angle of attack and compared to the classical “rigid mesh” approach. In the case of a CROR, such a simulation is basically a two-frequency simulation: one aft propeller blade is subject to an incidence effect at pulsation Ω, and to a front propeller wake effect at pulsation $2N_{front}\,\Omega$.

The following Figure 6 shows time evolutions of axial and vertical forces on front and rear single blade and on front and rear full propeller.

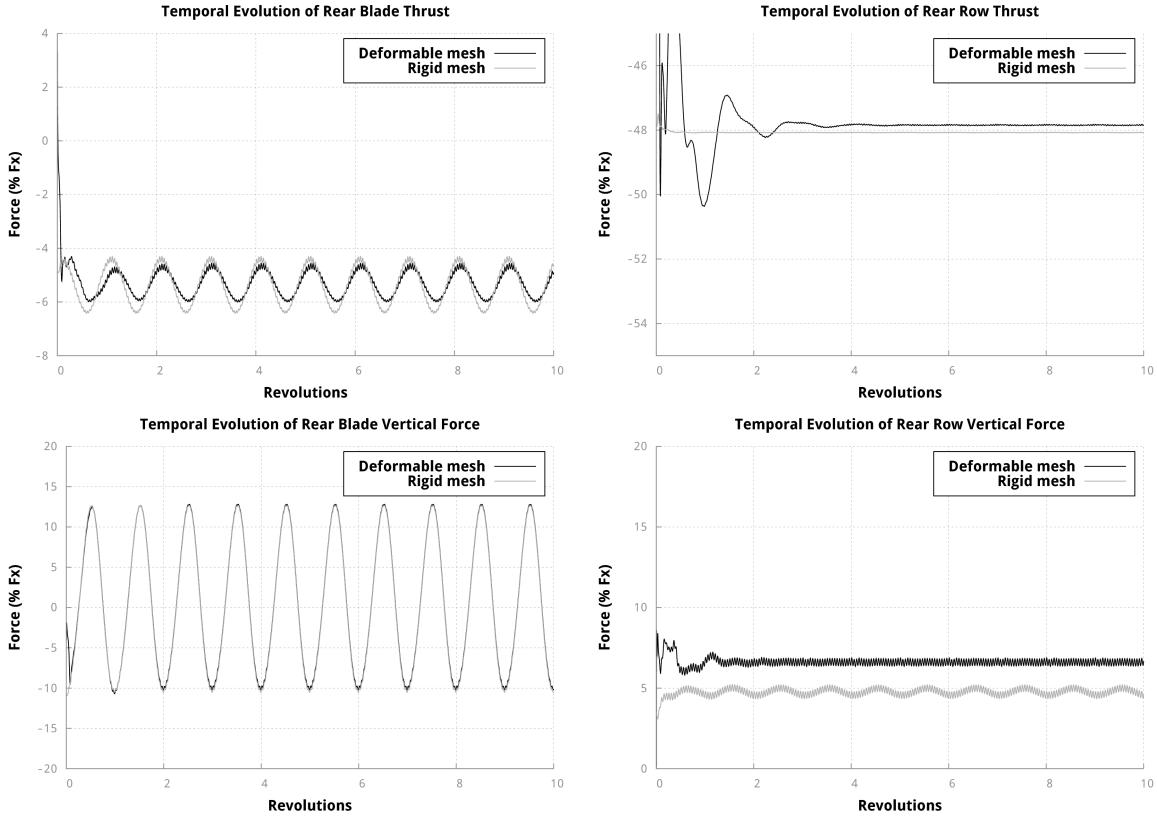

Figure 6: Comparison of forces for "rigid mesh" and "deformable mesh" approaches

Both approaches are in a good agreement on the high frequency amplitude and on both high and low frequency phases. Some discrepancies exist on the thrust force module but they are no bigger than 0.5% for both rows. A good agreement is found concerning blade vertical forces, but some small discrepancies exist at peak values (left bottom plot). The sum of these discrepancies leads to the difference between both approaches on propeller forces (right bottom plot).

High frequency amplitudes corresponding to the wake passing frequency also match well as it can be seen on Figure 7.

A yet unexplained behaviour of the “rigid mesh” computation leads to low frequency oscillations of vertical row forces, which is not predicted by the deformable approach.

Figure 7 shows the corresponding spectrum of forces shown on Figure 6.

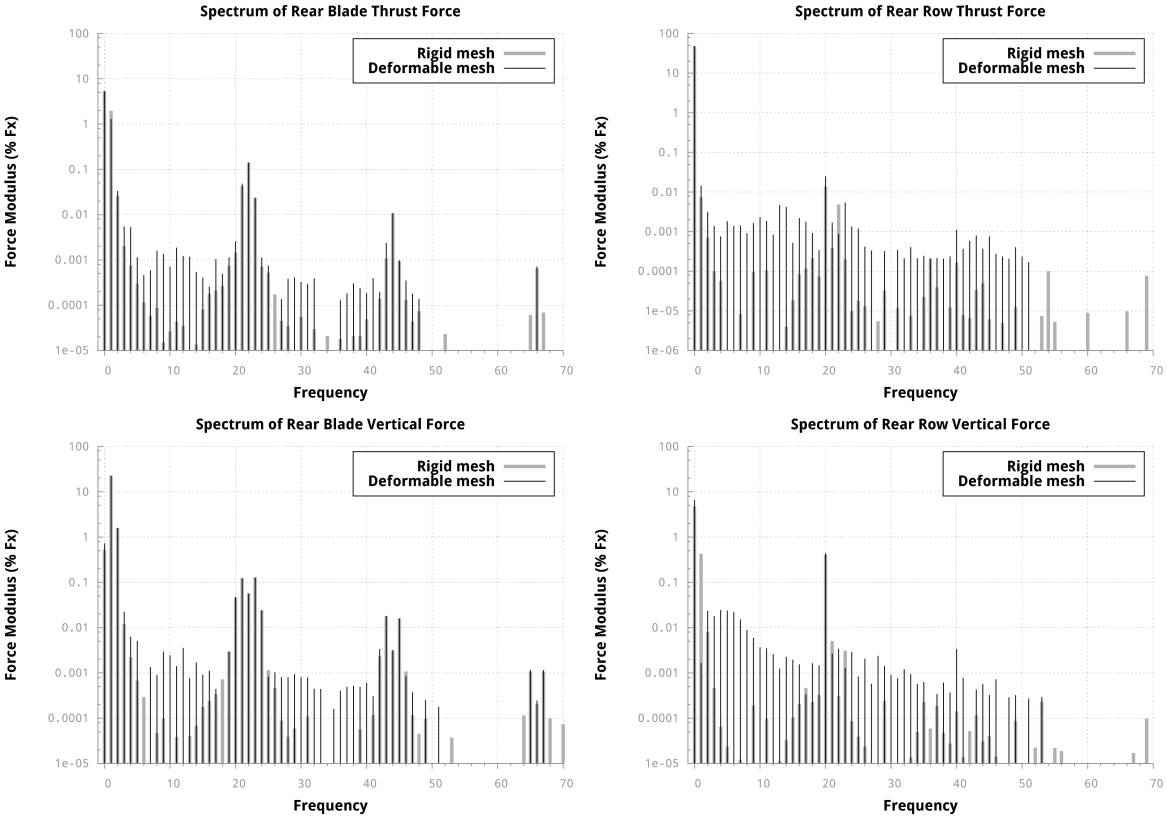

Figure 7: Comparison of forces spectra for "rigid mesh" and "deformable mesh" approaches

Spectra of blade axial and vertical forces match very well between both approaches, unless small modulus difference exists in particular for the first harmonic of axial force and for the mean value of vertical force, which correspond to the discrepancies previously described on the time history plot. On row forces, main peaks are predicted in good agreement by both methods, but the “rigid mesh method” exhibits a larger spectrum of intermediate frequencies.

The global good agreement between both computations allows validating the “deformable mesh” approach for the following whirl flutter simulations.

4.4 Whirl flutter effect

The previously described method has been implemented in the case of a whirl flutter motion on the AIPX7 CROR model at zero mean angle of attack and for a 1° motion amplitude at frequency $\omega = \frac{3}{4}\Omega$. This pulsation value has been chosen in order to get a strictly periodic signal over four rotation cycles.

Figure 8 and Figure 9 respectively show time evolutions of axial and transversal forces. On both figures, front and read blade and row are plotted. On Figure 8, subplots of full periodical signal are also plotted. This corresponds to the 4 last engine revolutions and to the 3 last whirl revolutions.

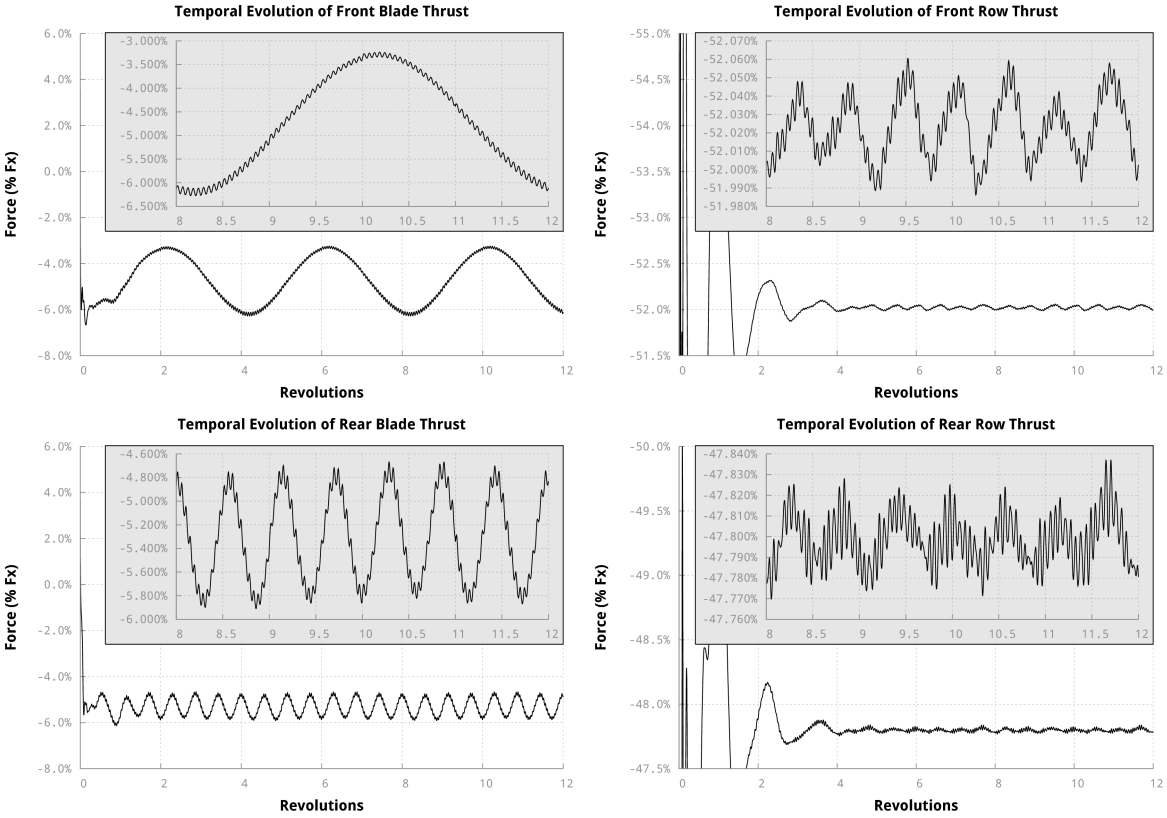

Figure 8: Time evolution of front and rear blade and row axial force

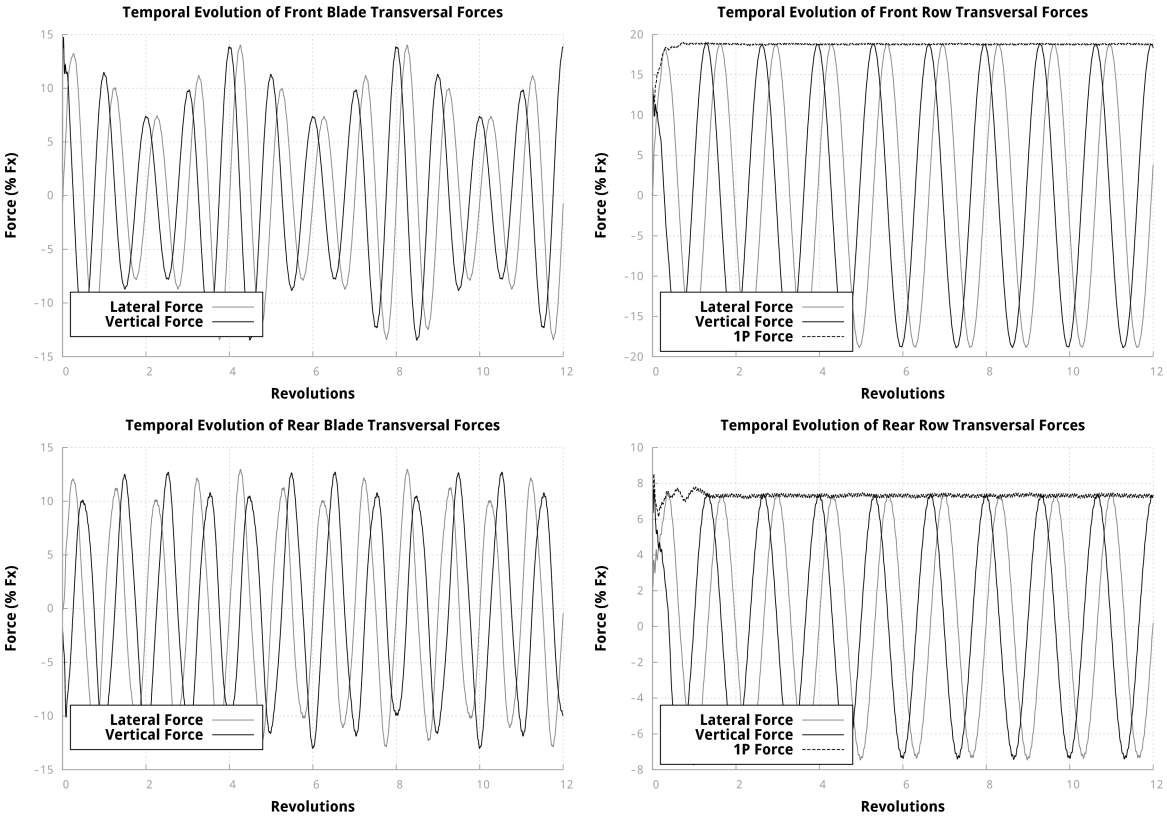

Figure 9: Time evolution of front and rear blade and row transversal forces

A good convergence level can be observed for all force components on both blades and propellers. The 1P force plotted on Figure 9 (propellers results) corresponds to the module of the transversal forces.

On the thrust front blade results, a 1-period signal can be observed on the 4 last engine revolutions. This is due to the fact that the front propeller pulsation has an opposite sign to the whirl pulsation. Thus, the motion of the front propeller is driven by the follow pulsation: $\Omega - \omega = \Omega - {}^{3}\!/_{4}\,\Omega = {}^{1}\!/_{4}\,\Omega$. But, on the rear blade thrust plot, a 7-period signal can be observed which corresponds to the pulsation: $\Omega + \omega = \Omega + {}^{3}\!/_{4}\,\Omega = {}^{7}\!/_{4}\,\Omega$. Opposite row motion influence is visible on time history thrust plots, which exhibit additional high frequency oscillations.

For both front and rear propellers, the total thrust oscillations observable on Figure 8 are not significant compared to the absolute value of the thrust. The average thrust of the front propeller is stabilized to 51.95% and 47.73% for the thrust rear propeller. The row thrust diagrams however present a multi-frequency content to be analysed (see below).

Figure 10 and Figure 11 show spectra of rear single blade and rear full propeller force components. All force components are analysed using a Fast Fourier Transformation in order to get them in the spectral domain. The frequencies are presented in term of multiple of the CROR rotation frequency.

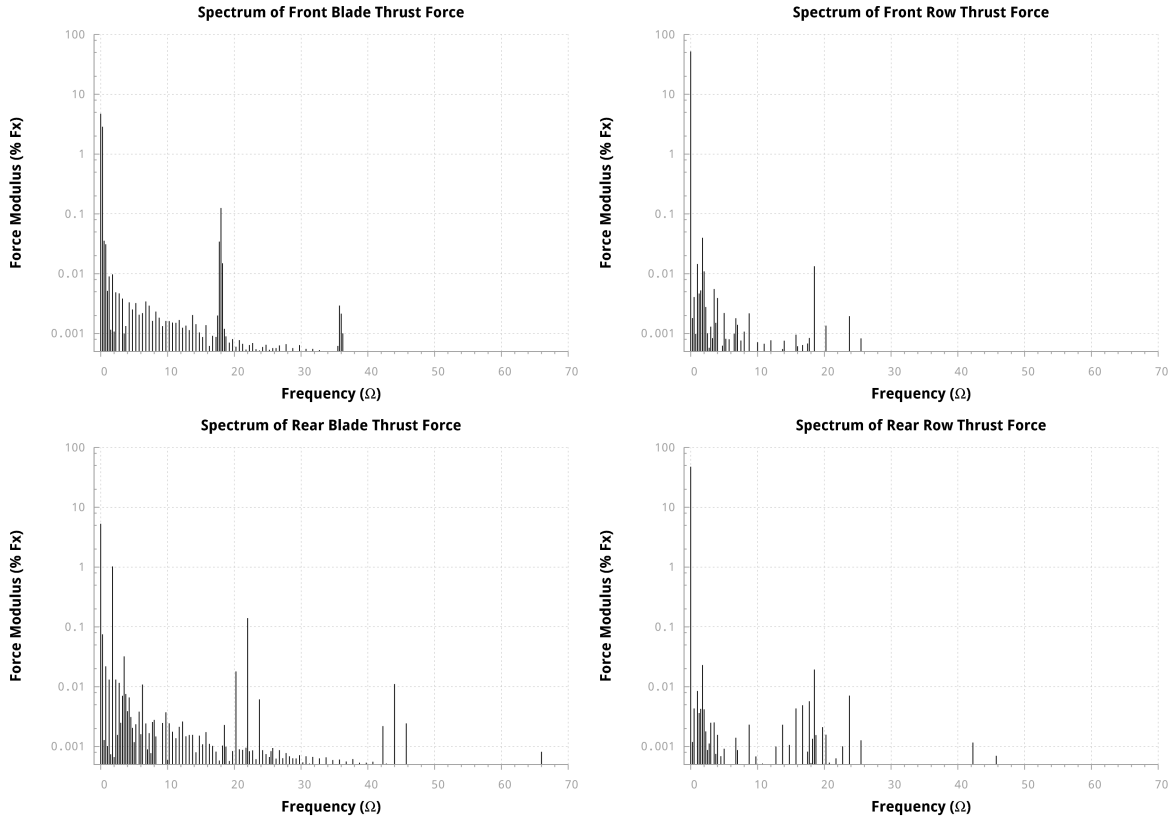

Figure 10: Spectra of front and rear blade and row thrust

The mean component sum up on the propeller, which is not the case for other frequencies ($\omega, 22\Omega, \ldots$) which vanish on the full row except for the peak at ($20\Omega - 2\omega$) (which is present but whose level appears unnoticeable in the single blade spectrum).

On Figure 11, the sum of the first blade peak (ω) over the row produces a vertical force about 10 times larger, while the largest peak on the blade (Ω) vanishes when it is summed over the row. Once again, the only high frequency existing on the row is $20\Omega - \omega$ which corresponds to the first of the six peaks existing from $20\Omega - \omega$ to $23\Omega + \omega$ on the blade. All others peaks vanish when summed up over the whole row.

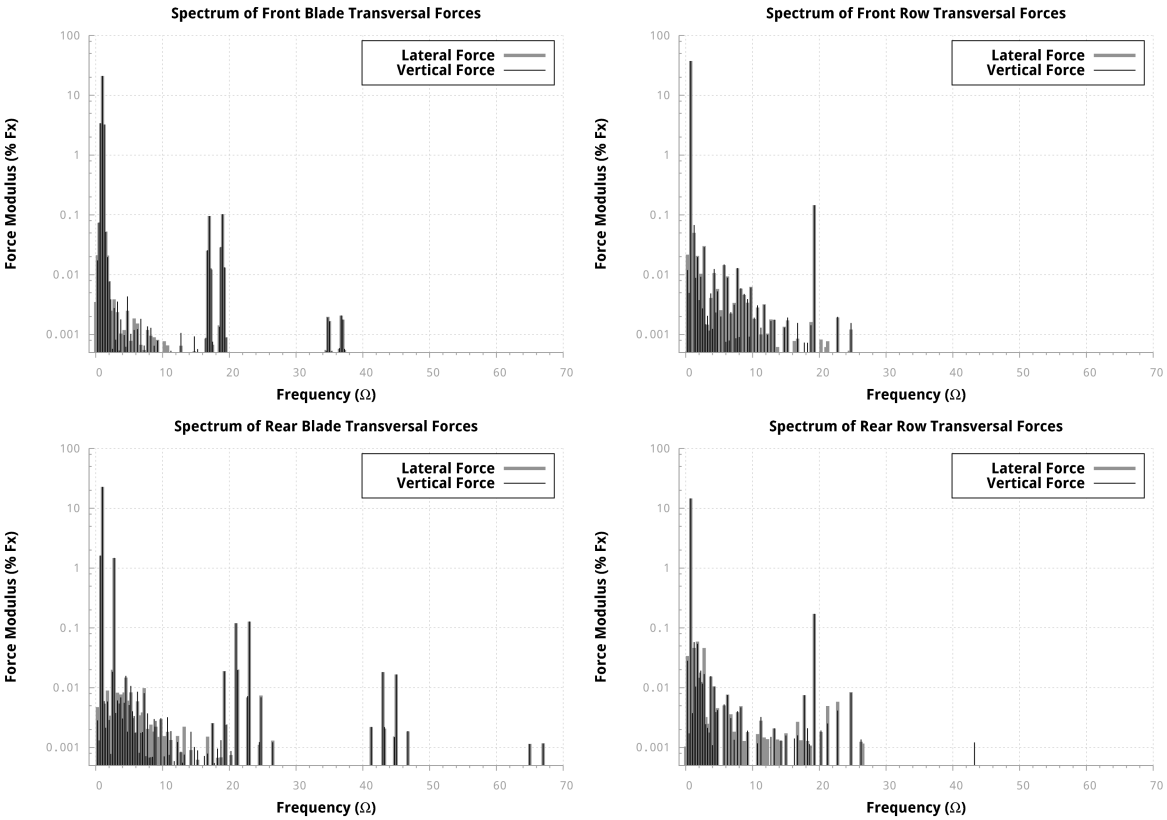

Figure 11: Spectra of rear blade vertical force vs rear row vertical force

4.5 Load spectrum analysis using a simple analytical model

A simple analytical model has been developed for a better understanding of the CFD results. This model is based on basic geometrical considerations and a simple aerodynamic force model giving blade b aerodynamic force $\vec{F}_b$.

$$\vec{F}_b = \frac{1}{2}\rho S V_{\infty/Rb}^2 C_{z\alpha}\alpha_b \vec{n_b} \qquad \overrightarrow{V_{\infty/Rb}} = V_\infty \vec{X} + \Omega r \vec{t_b}$$

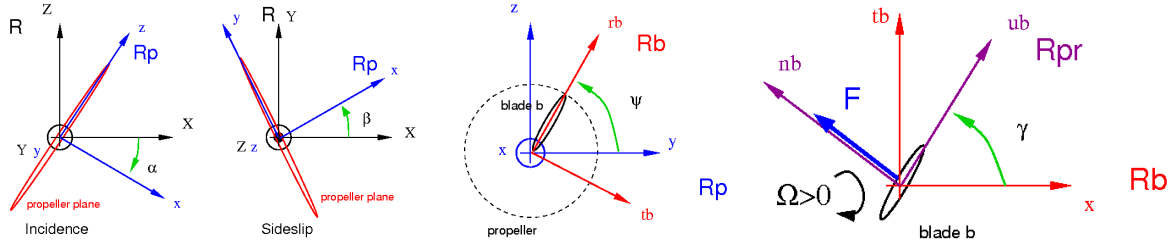

Figure 12: Propeller, blade and airfoil frames

Correction multiplicative terms on blade airfoil impinging velocity $\overrightarrow{V_{\infty/Rb}}$ are implemented in order to take into account velocity perturbations effects due to nacelle incidence (ν_{AoA}) and front blade wake (ν_{wake}) passing. In case of whirl precession motion these terms may be written as:

$$\nu_{AoA}(b) = (1+\varepsilon\cos[\psi_b(t)-\psi_{Wh}(t)]) \qquad \nu_{wake}(b) = (1+w\sin(2N_{Front}\Omega t + N_{Front}\psi_b^0))$$

where ε and w respectively size the corrective terms for nacelle incidence and front blade wake effects, these corrective coefficients being small (<<1).

This model allows to access to the force frequency content on single blade and full propeller (possibly including mistuning). However, due to the coarse level of the aerodynamic modelling, absolute levels are not relevant and corrective terms needs to be adjusted for each model in order to

fit to CFD peaks level. Figure 13 shows spectra of vertical blade and row forces predicted by this model, and compared to those given by CFD.

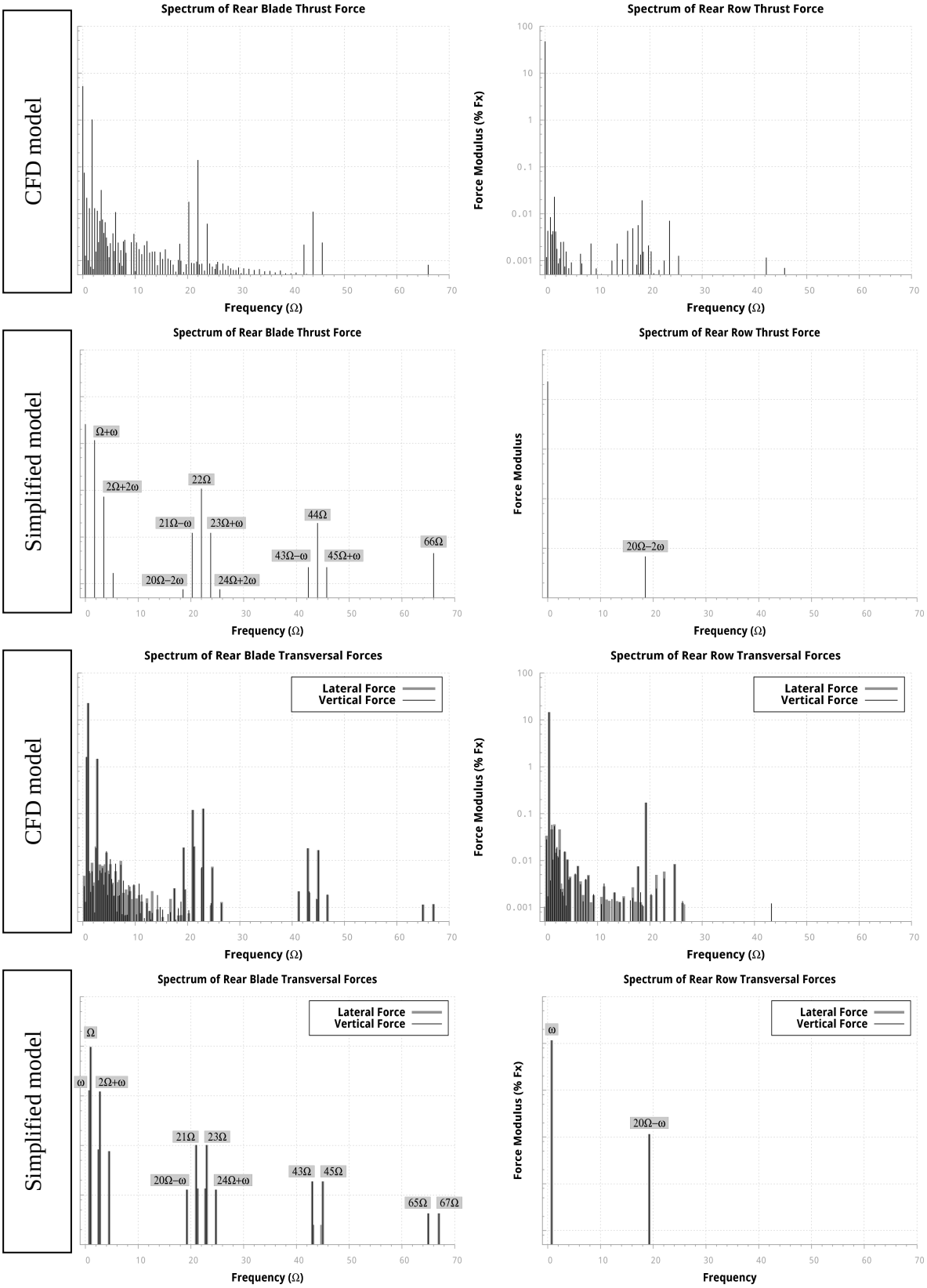

Figure 13: Spectra of analytical model vertical blade and row forces

Surprisingly, the predicted spectra compare well to the High Fidelity CFD results. Frequency peaks are in good agreement with those given by CFD, and even though absolute levels differ, the relative ordering of force levels seems to be in good accordance with CFD also.

In addition, a first order analysis may be conducted on analytical force terms, for small values of whirl precession amplitude α_m, and of the corrective terms ε and w. It can be derived in closed form that for a perfectly tuned propeller only force terms occurring on the single blade at a frequency multiple of $N_{Aft}\Omega$ are present in the full row spectrum. Therefore, only few peaks occurring on the blade are allowed to sum up on the full row, whereas many of them are to vanish.

In the case of vertical forces, the following table is obtained, sorting frequency response terms, for both aft blade and aft propeller forces:

Amplitude	Blade Freq	Propeller Freq
1.	Ω	vanishes
α_m	ω	ω
ε	$2\Omega-\omega, \omega$	vanishes
w	$(2N_{Front}\pm1)\Omega$	$(2N_{Front}\pm1)\Omega$ if $N_{Front}\pm1=kN_{Aft}$
$\alpha_m\varepsilon$	$\Omega, \Omega-2\omega$	vanishes
$\alpha_m w$	$2N_{Front}\Omega\pm\omega$	vanishes
εw	$2N_{Front}\Omega\pm\omega$ $(2N_{Front}\pm2)\Omega\mp\omega$	$(2N_{Front}\pm2)\Omega\mp\omega$ if $N_{Front}\pm2=kN_{Aft}$
$\alpha_m\varepsilon w$	$(2N_{Front}\pm1)\Omega$ $(2N_{Front}\pm1)\Omega\mp2\omega$	$(2N_{Front}\pm1)\Omega\mp2\omega$ if $N_{Front}\pm1=kN_{Aft}$

Table 1 : Vertical forces on aft propeller frequency content analysis

Similar results may be obtained for axial and side forces, which are not detailed here.

In the case of whirl precession motion presented above, this allow to confirm the vanishing of all peaks of the blade on the row except for the two ω and $20\Omega-\omega$ peaks which is due to the combination on the row of the delayed blades signals for specific values of propeller blade numbers (here $N_{Front}-2=N_{Aft}$). One may notice that the second emerging peak on row are not the first order levels observed on blade spectrum, but only a second order term, coupling nacelle incidence and wake effect corrective terms (εw). It can also be understood from this analysis that the structure of the full row spectrum is likely to become different than the one observed here, for another (N_{Front}, N_{Aft}) CROR blade numbering.

5 ONGOING ACTIVITY

5.1 Whirl flutter stability analysis

Additional activity is scheduled. First, whirl flutter stability analysis must be conducted, using the evaluation of dynamic loads encountered during rigid motions of the CROR, as detailed above, and also the structural dynamic characteristics of the engine.
The structural dynamics equation for the rotating engine reads:

$$\mu_s\ddot{q}+(\beta_s+G)\dot{q}+\gamma_s q-\Phi^t F_A(t)=0$$

where G is the antisymmetric gyroscopic damping matrix

$$G=\Omega J_X \mathbf{J} \quad \mathbf{J}=\begin{bmatrix}0 & 1\\ -1 & 0\end{bmatrix}$$

Generalized aerodynamic forces are classically linearized with respect to generalized coordinates: $\Phi^t F_A(t)=\mathbf{A}q+\mathbf{B}\dot{q}$. The involved generalized forces matrices are built by projecting

the aerodynamic unsteady forces on the rigid body motion basis (pitch and yaw motions), obtained as developed in the above sections.
The stability analysis of pitch/yaw combined motion is then conducted in considering the following generalized coordinates damped harmonic motion, where pitch and yaw motion may be out of phase.

$$q = q^* e^{pt}, \quad \dot{q} = pq, \quad \ddot{q} = p^2 q, \quad p = j\omega(1 + j\alpha)$$

The stability of the combined motion is deduced from the sign of the real part of the p_i eigenvalues of the eigen problem resulting from the structural dynamics equations:

$$\left[p^2 \mu_s + p(\beta_s - \mathbf{B} + \Omega J_X \mathbf{J}) + \gamma_s - \mathbf{A} \right] q = 0$$

The impact of the antisymmetric gyroscopic damping matrix is to lead to out of phase combined pitch and yaw eigen modes, whereas aerodynamic terms may introduce negative damping, leading to whirl flutter unstable modes.

5.2 Unsteady loads prediction for installed configurations

The second ongoing activity concerns the unsteady loads prediction for installed CROR configurations.The current objective is now to evaluate unsteady aerodynamic forces for a pylon mounted CROR configuration. In this case, additional difficulties occur for the numerical modelling, because deformation of the pylon must be taken into account as well as the motion of the engine.

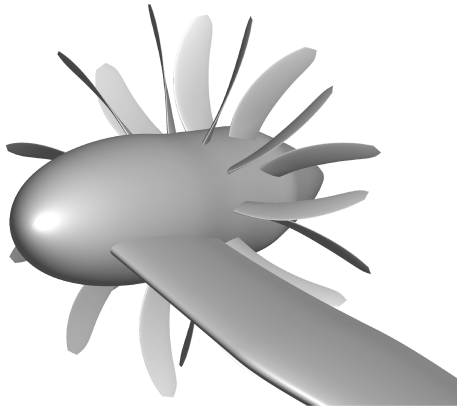

Figure 14: AIPX7 CROR installed configuration

6 CONCLUSION

A specific numerical method to predict aerodynamic forces occurring on Counter Rotating Open Rotor in whirl flutter motion has been presented in this paper.

The analytical investigation of this specific motion has been presented. An original approach allowing the simulation of this prescribed whirl flutter motion using a deformable mesh approach and rotating modes of deformation has been presented and implemented in the *elsA* CFD software. Several simulations have been performed, including static incidence, pitch and whirl flutter precession motion.
Force time history and spectra occurring on the CROR have been presented and discussed. They have been compared to a simple analytical model, which is not able to predict accurate levels but gives comparable frequency content, allowing going further in the comprehensive analysis.

The next step of this work is to perform aircraft installed CROR simulations of whirl flutter motion. Simulations of whirl flutter with deformable blades could be a second interesting perspective which is already allowed by the chosen approach.

The present study has been done thanks to the support of DGA, DGAC and AIRBUS FRANCE.

7 REFERENCES

[1] CAMBIER L., HEIB S., PLOT S., *The ONERA elsA CFD software: Input from Research and Feedback from Industry*, ICAS 2012, 23 - 28 September, 2012, Brisbane, Australia.
[2] GIRODROUX-LAVIGNE P., *Fluid-Structure Coupling Using Chimera Grids*, International Forum on Aeroelasticity and Structural Dynamics, 21-25 June 2009, Seattle, USA.
[3] DUGEAI A., MAUFFREY Y., SICOT F., *Aeroelastic capabilities of the elsA solver for rotating machines applications*, IFASD 2011, paper 079, Paris, June 2011
[4] PLACZEK A., DUGEAI A., *Numerical prediction of the aeroelastic damping using multi-modal dynamically coupled simulations on a 360° fan configuration,* IFASD 2011, paper 084, Paris, June 2011
[5] SICOT F., DUGEAI A.., *Numerical Investigation of Propellers Whirl Flutter using elsA*, IFASD 2011, paper 177, Paris, June. 2011.